Ocean Engineering 291 (2024) 116509

Contents lists available at ScienceDirect

Ocean Engineering

journal homepage: www.elsevier.com/locate/oceaneng

The application of the coupled acoustic–structural approach (CASA) method on the free vibration of submerged structures

Oskar Ask Ullestad [a], Zhenhui Liu [b,c,*]

[a] Department of Physics and Technology, University of Bergen, Norway, 5007, Bergen, Norway
[b] Engineering Consultancy, Department of New Energy, Aker Solutions AS, Norway, 7435 Trondheim, Norway
[c] Department of Mechanical and Marine Engineering, Western Norway University of Applied Sciences, Norway, 5528, Haugesund, Norway

ARTICLE INFO

MSC:
00-01
99-00

Keywords:
Free vibration
Modal analysis
Submerged structures
CASA
Acoustic elements
FEM

ABSTRACT

Traditionally, the consideration of the surrounding water during the modal analysis of submerged structures has been done by applying constant added mass factors. This method may lose its accuracy for complicated structures, especially those with bends and multi-plane topology. The present study utilizes the coupled acoustic structural approach (CASA) to obtain natural frequencies on submerged structures. The work compares the simulated CASA results with experimental results. Four experiments with objects with different geometry were chosen; a straight pipe, cantilever plates, stiffened cylindrical shell, and a disk. We found that the CASA method produced accurate results for the three first eigenmodes compared to the experimental results. It could simulate bending, twisting, ovality, and stretching mode shapes with an accuracy of less than 10 % difference. Additionally, we applied the CASA method to two submerged jumper structures for the first time. We found that the CASA method gives accurate modal analysis results and is recommended for use.

1. Introduction

Determining a structural system's natural frequencies and mode shapes is paramount in forecasting its reaction to external dynamic loads, including earthquakes, explosions, or wind-induced vibration (WIV). When an object oscillates at or close to its natural frequency, resonance occurs, resulting in substantial structural impairment. Consequently, modal analysis is frequently indispensable during a project's design and maintenance stages.

Numerous engineering disciplines, such as naval architecture, noise control, vibration isolation, offshore structures, dam-reservoir structures, and nuclear plants, demonstrate a keen interest in accurately determining the natural frequencies of fluid–structure interaction fluid–structure interaction (FSI) phenomena (Bak and Yoo, 2019; Chae and Kim, 2010; Cheng et al., 2015; Liu et al., 2019; Fourey et al., 2017; Hellgren, 2014; Fujita, 1990). In the case of submerged structures, the presence of surrounding water introduces additional complexities. Conventionally, modal analysis employs a simplified technique incorporating a constant added mass factor to account for the water effect. However, this approach oversimplifies the problem.

The fatigue assessment resulting from vortex-induced vibration (VIV) necessitates the incorporation of the free vibration characteristics of subsea jumpers. Liu et al. (2019) highlight the significance of these characteristics. Conventionally, commercial software such as ANSYS/ABAQUS or similar tools employs beam elements to simulate subsea jumpers, including bends. However, recent findings by Sieber et al. (2021) indicates that the beam elements may inaccurately predict the free vibration modes in the presence of bends.

Several experiments have investigated the vibration of structures underwater. Lindholm et al. (1962) studied the vibration of cantilever plates in air and water. Razi and Taheri (2014) experimented with a laboratory tank to measure the eigenvalues of a straight pipe submerged in water. Valentín et al. (2017) performed tests on a rig that involved a stainless steel disk attached to a shaft and placed in an aluminum tank filled with water. In Gao et al. (2022), a typical stiffened cylindrical shell's vibration and sound radiation under broad excitation were measured underwater. ExxonMobil (Wang et al., 2013) conducted model tests using an M-shaped jumper model to evaluate the accuracy of potential VIV prediction methods. They simulated constant bottom currents to achieve lower velocities that activate the relevant vibration modes.

The concept of added mass has also been used to idealize the influences of the surrounding water (FSI) (Peng and Hao, 2012; Peng et al., 2012; Zhu et al., 2008; Bao et al., 2013). Blevins (2001) formulated the added mass term as a velocity potential function around vibrating

* Corresponding author at: Department of Mechanical and Marine Engineering, Western Norway University of Applied Sciences, Norway, 5528, Haugesund, Norway.
E-mail addresses: oskarask.ullestad@dof.com (O.A. Ullestad), zhenhui.liu@akersolutions.com, zhenhui.liu@outlook.com (Z. Liu).

https://doi.org/10.1016/j.oceaneng.2023.116509
Received 12 August 2023; Received in revised form 30 October 2023; Accepted 1 December 2023
Available online 8 December 2023
0029-8018/© 2023 The Author(s). Published by Elsevier Ltd. This is an open access article under the CC BY license (http://creativecommons.org/licenses/by/4.0/).

structures and showed that it could only be formulated when there are mathematical solutions.

Kramer et al. (2013) used the "added-mass" concept. They first examined a submerged beam's vibration and the natural vibration of composite plates beneath the surface. An analysis was conducted on the free vibrations of a composite cantilever plate in both air and water. The study used an analytical model based on composite strip theory, beam theory, and a numerical model called coupled acoustic–structure approach (CASA). The results showed that the wetted frequencies were lower than the dry frequencies due to added mass effects.

Zeinoddini et al. (2012) focused on the seismic behavior of a free-spanning submarine pipeline. They used a numerical finite-element model and compared its results to those obtained through a traditional added mass approach and a more complex CASA method. Their findings showed that the simplified added mass method typically underestimated the pipeline response in a free-spanning situation compared to the responses obtained through the CASA.

CASA has also been used in vibration-based structural health monitoring (VB-SHM) in recent years (Chen and Su, 2009). Razi and Taheri (2015) aimed to enhance our understanding of modeling and essential parameters related to simulating vibration in submerged pipes, with a focus on utilizing VB-SHM techniques. The study explored two methods commonly used to model how submerged structures respond to dynamic forces. These methods were the "added mass approach" and "CASA". They found that the differences between the two methods were minimal for lateral bending modes at less than 2 %. However, the differences were closer to 20 % for the torsional mode. This significant difference was due to the limitations of the added mass approach. Therefore, the CASA was recommended for successful VB-SHM of submerged structures.

Ross et al. (2007) found noticeable decreases in the eigenvalues of a urethane prolate underwater and exposed to changing external pressure. However, Zou et al. (2005) reported minimal change in the bending eigenvalues of a composite pipe when subjected to varying internal pressure.

This paper comprehensively evaluates the CASA method in modal analysis. ABAQUS (Smith, 2009) is used to do the simulation due to its substantial flexibility in handling the interface between acoustic and structural elements. Additionally, we present two application cases with two subsea jumpers in which bends and multi-plane topology are included.

This paper is organized as follows: Section 2 presents the relevant theory and methodology, and Section 3 presents the validation cases. In Section 4, two application examples are presented, and the results are discussed. A brief discussion on the cost-effectiveness of CASA method is presented in Section 5. Finally, the conclusions are given in Section 6.

2. Related theory for the interaction between acoustic medium and structures

2.1. Weak form for coupled systems

When dealing with an acoustic medium, it is possible to solve for free vibration using numerical methods such as applying the standard Galerkin discretization approach, as explained in Zienkiewicz (2005). For visual reference, Fig. 1 displays a straightforward example of a structural domain encompassed by an acoustic medium.

The weak form represents acoustic medium dynamics as follows:

$$\delta \prod_f = \int_{\Omega_f} \delta p \left[\frac{1}{c^2} \ddot{p} - \nabla^2 p \right] d\Omega = 0 \tag{1}$$

where p is the pressure and c is given by

$$c = \sqrt{\frac{K}{\rho_0}} \tag{2}$$

where K is the bulk modulus of the fluid, and ρ_0 is the density in the hydrostatic state. By integrating by parts, Eq. (1) can be expanded to the following equation

$$\begin{aligned} \int_{\Omega_f} \left[\delta p \frac{1}{c^2} \ddot{p} - (\nabla \delta p)^T (\nabla p) \right] d\Omega + \int_{\Gamma_1} \delta p \rho_0 n^T \ddot{u} d\Gamma \\ + \int_{\Gamma_3} \delta p \frac{1}{c} \dot{p} d\Gamma + \int_{\Gamma_4} \delta p \frac{1}{c} \dot{p} d\Gamma = 0 \end{aligned} \tag{3}$$

where Ω_f is the fluid domain, ρ_f is the fluid density, and Γ_i is the integral over the boundary part. To solve Eq. (3) for a discrete domain, an approximation is made for the displacement and nodal acoustic pressure

$$\begin{aligned} \mathbf{u} &\approx \mathbf{N}_u \tilde{\mathbf{u}} \\ p &\approx \mathbf{N}_p \tilde{\mathbf{p}} \end{aligned} \tag{4}$$

The nodal parameters for each field are represented by $\tilde{\mathbf{u}}$ and $\tilde{\mathbf{p}}$, and the appropriate shape functions are denoted by $\mathbf{N}_u$ and $\mathbf{N}_p$. This results in a discrete structural problem as

$$\mathbf{M}\ddot{\tilde{\mathbf{u}}} + \mathbf{C}\dot{\tilde{\mathbf{u}}} + \mathbf{K}\tilde{\mathbf{u}} - \mathbf{Q}\tilde{\mathbf{p}} + \mathbf{f} = \mathbf{0} \tag{5}$$

The coupling term appears as a result of the specified pressures on the boundary as

$$\int_{\Gamma_t} \delta \mathbf{N}_u^T \bar{\mathbf{t}} d\Gamma = \mathbf{Q}\tilde{\mathbf{p}} \tag{6}$$

and

$$\mathbf{S}\ddot{\tilde{\mathbf{p}}} + \tilde{\mathbf{C}}\dot{\tilde{\mathbf{p}}} + \mathbf{H}\tilde{\mathbf{p}} + \rho_f \mathbf{Q}^T \ddot{\tilde{\mathbf{u}}} = \mathbf{0} \tag{7}$$

where

$$\begin{aligned} \mathbf{Q} &= \int_{\Gamma_t} \delta \mathbf{N}_u^T \mathbf{n} \mathbf{N}_p d\Gamma n \\ \mathbf{S} &= \int_{\Omega_f} \mathbf{N}_p^T \frac{1}{C^2} \mathbf{N}_p d\Omega \\ \tilde{\mathbf{C}} &= \int_{\Gamma_f} \mathbf{N}_p^T \frac{1}{C} \mathbf{N}_p d\Gamma \\ \mathbf{H} &= \int_{\Omega_f} \left(\nabla \mathbf{N}_p \right)^T \nabla \mathbf{N}_p d\Omega \end{aligned} \tag{8}$$

Matrices can be used to represent the free vibration of the coupled system. When only considering free vibrations and ignoring force and damping terms (except for radiation energy loss in the fluid component), the two equations Eq. (5) and Eq. (7) can be combined into a set as

$$\begin{bmatrix} \mathbf{M} & \mathbf{0} \\ \rho_0 \mathbf{Q}^\mathbf{T} & \mathbf{S} \end{bmatrix} \begin{bmatrix} \ddot{\tilde{\mathbf{u}}} \\ \ddot{\tilde{\mathbf{p}}} \end{bmatrix} + \begin{bmatrix} \mathbf{K} & -\mathbf{Q} \\ \mathbf{0} & \mathbf{H} \end{bmatrix} \begin{bmatrix} \tilde{\mathbf{u}} \\ \tilde{\mathbf{p}} \end{bmatrix} = \mathbf{0} \tag{9}$$

The problem above is comparable to the one that occurs in the vibration of rotating solids. After some substitution and manipulation, Eq. (9) can be written as

$$\left(\begin{bmatrix} \mathbf{K} & \mathbf{0} & \mathbf{0} \\ \mathbf{0} & \frac{1}{\rho_0}\mathbf{S} & \mathbf{0} \\ \mathbf{0} & \mathbf{0} & \mathbf{0} \end{bmatrix} - \omega^2 \begin{bmatrix} \mathbf{M} & \mathbf{0} & \mathbf{Q} \\ \mathbf{0} & \mathbf{0} & \frac{1}{\rho_0}\mathbf{S} \\ \mathbf{Q}^T & \frac{1}{\rho_0}\mathbf{S}^T & -\frac{1}{\rho_0}\mathbf{H} \end{bmatrix} \right) \begin{pmatrix} \check{\mathbf{u}} \\ \check{\mathbf{p}} \\ \check{\mathbf{q}} \end{pmatrix} = \mathbf{0} \tag{10}$$

Which is a symmetric generalized eigenvalue problem.

2.2. Structure–acoustic medium contact in ABAQUS

In this study, we utilized the CASA from the commercial code ABAQUS (Smith, 2009). The surface-based method is chosen for meshes with different node numbering and non-coincident surface meshes. It is also simpler and less computationally expensive than the element-based approach.

This method calculates forces on the surfaces of structural and acoustic media. An interpolated point force from one surface (the "master") is applied to the other surface (the "slave"). When dealing

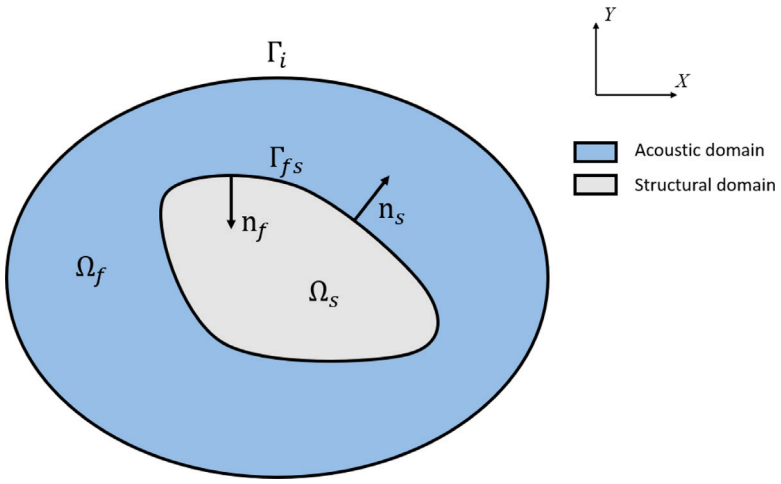

Fig. 1. Acoustic domain Ω_f and structural domain Ω_s coupled by integrals over the acoustic–structure interface Γ_{fs} and radiation boundary Γ_i.

with solid elements, the medium with the higher wave speed should be the master surface, except in cases where fluids are coupled to both sides of beam or shell elements.

The mesh for the medium with the lower wave speed (usually the fluid) should generally be more refined to capture the details of the acoustic wave propagation accurately. The medium with the more refined mesh should be designated as the slave surface in the simulation. The nodal points on this surface will enforce the coupling between the acoustic and structural domains. Suppose the wave field near the fluid–solid interface is of particular importance. In that case, it is possible to have both meshes (fluid and solid) equally refined, with the refinement level corresponding to the lower wave speed medium. In this case, the choice of the master surface is somewhat arbitrary.

When fluids are coupled to both sides of shell or beam elements, it is an exception because it introduces specific modeling challenges and considerations that differ from the typical acoustic–structure interaction scenarios where one side is a solid medium. The other side is a fluid medium. In such scenarios, the requirements for element sizes and meshing can be different from standard acoustic–structure interactions due to the unique characteristics of shell and beam elements.

The expression for the CASA problem concerning the acoustic medium is

$$\begin{aligned}&\int_{V_f}\left[\delta p\left(\frac{1}{K}\ddot{p}+\frac{r\gamma}{\rho_f K}\dot{p}\right)+\frac{1}{\rho_f}\frac{\partial\delta p}{\partial\mathbf{x}}\cdot\frac{\partial p}{\partial\mathbf{x}}\right]dV_f\\&+\int_{S_{fs}\bigcup S_{frs}}\delta p\bar{\mathbf{n}}\cdot\frac{\partial p}{\partial\mathbf{x}}dS-\int_{S_{ft}}\delta p a_{in}dS\\&+\int_{S_{fs}\bigcup S_{frs}}\delta p\left(\frac{\gamma}{\rho_f c_1}p+\left(\frac{\gamma}{\rho_f k_1}+\frac{1}{c_1}\right)\dot{p}+\frac{1}{k_1}\ddot{p}\right)=0\end{aligned}\tag{11}$$

and the structural behavior is defined by the virtual work equation

$$\begin{aligned}&\int_V\delta\varepsilon:\boldsymbol{\sigma}dV+\int_V\alpha_c\rho\delta\mathbf{u}^m\cdot\dot{\mathbf{u}}^m dV+\int_V\rho\delta\mathbf{u}^m\cdot\ddot{\mathbf{u}}^m dV\\&\quad+\int_{S_{fs}\bigcup S_{frs}}\delta\mathbf{u}^m\cdot\bar{\mathbf{n}}pdS-\int_{S_t}\delta\mathbf{u}^m\cdot\mathbf{t}dS=0\end{aligned}\tag{12}$$

The formula comprises numerous variables and terms, incorporating information regarding pressure p, fluid density ρ_f, bulk modulus K, normal vector $\bar{\mathbf{n}}$, acoustic-medium motion S_{fs}, acoustic–structural boundary S_{frs}, fluid impedance integral $S_{fs}\bigcup S_{frs}$, the spatial position of the fluid particle $\mathbf{x}$, variational displacement field $\mathbf{u}^m$, the velocity of a point in the structure $\dot{\mathbf{u}}^m$, acceleration of a point in the structure $\ddot{\mathbf{u}}^m$, spring parameter k_1, dashpot parameter c_1, volumetric drag γ, strain variation compatible with $\mathbf{u}^m$ $\delta\epsilon$, stress at a point in the structure $\boldsymbol{\sigma}$, mass-proportional damping factor α_c, and surface traction applied to the structure $\mathbf{t}$.

The primary interests are the terms integrated over the combined areas of fluid and fluid–solid surfaces, denoted as $S_{fs}\bigcup S_{frs}$. These terms depend solely on the acoustic pressure field and its variations and remain constant when in contact with a solid. Fluid nodes designated as slaves are calculated by averaging their neighboring master surface nodes' values. Fig. 2 showcases the nodes.

Fig. 2 identifies $\mathbf{x}_N$ as the slave nodes' projections onto the master surface, A_N as their areas, and $\mathbf{P}(\mathbf{x}_N)$ as their projection points on the master surface. The variables of the slave nodes, represented as $\mathbf{x}_N$, are determined by interpolating the variables from the nearby master surface nodes identified by the projection $\mathbf{P}(\mathbf{x}_N)$. By adding displacement degrees of freedom to the fluid slave surface, the pointwise fluid–solid coupling condition

$$\frac{1}{\rho_f}\frac{\partial p}{\partial\mathbf{x}}\cdot\bar{\mathbf{n}}+\ddot{\mathbf{u}}^m\cdot\bar{\mathbf{n}}=0\tag{13}$$

is enforced at the slave nodes. The master displacements restrict the slave displacements, which are then eliminated. This approximation enables the calculation of the fluid equation coupling term on the slave node level as

$$\int_{S_{fs}\bigcup S_{frs}}\delta p\bar{\mathbf{n}}\cdot\frac{\partial p}{\partial\mathbf{x}}dS=\int_{S_{fs}\bigcup S_{frs}}\delta p\bar{\mathbf{n}}\cdot\ddot{\mathbf{u}}^m dS\tag{14}$$

The term in Eq. (14) is derived by interpolating values of structural displacements at nearby master nodes times the slave node's area, as

$$\int_{S_{fs}\bigcup S_{frs}}\delta p\bar{\mathbf{n}}\cdot\ddot{\mathbf{u}}^m dS=A_N\left[\sum_i\bar{\mathbf{n}}(\mathbf{x}_n)\cdot N^i(\mathbf{p}(\mathbf{x}_n))\ddot{\mathbf{u}}_i^m\right]\tag{15}$$

where the master surface interpolant at the slave node projection is defined as $N^i(\mathbf{p}(\mathbf{x}_n))$, the acceleration of the structure at the master nodes is represented by $\ddot{\mathbf{u}}_i^m$, while the normal vector pointing into the fluid is calculated at the slave node as $\bar{\mathbf{n}}(\mathbf{x}_n)$. The sum includes all master nodes i that are close to the projection of the slave node, as shown in Fig. 2. The pressure coupling term is estimated by using the following formula.

$$\int_{S_{fs}\bigcup S_{frs}}\delta\mathbf{u}^m\cdot\bar{\mathbf{n}}dS=p_N A_N\left[\sum_i\bar{\mathbf{n}}(\mathbf{x}_n)\cdot N^i(\mathbf{p}(\mathbf{x}_n))\right]\tag{16}$$

where p_N represents the acoustic pressure at the slave node.

3. Validation of the CASA modeling with experimental tests

This section presents the validation of the implemented CASA models in ABAQUS. Four experiments have been tested, and the results are summarized and discussed.

Mesh refinement studies decided the element sizes. For each case, five mesh schemes were used to determine the optimal number of elements for accuracy and computational efficiency (mainly accuracy).

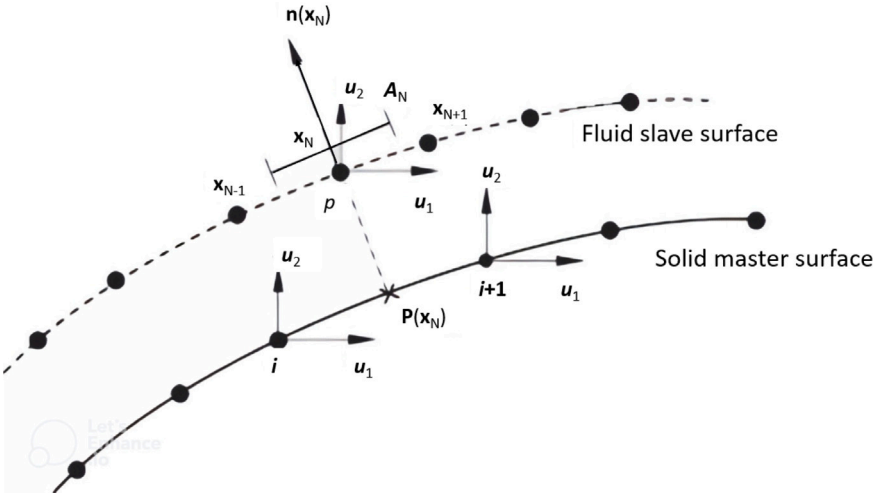

Fig. 2. Illustration of slave and master surfaces on the interface between fluid and solid.

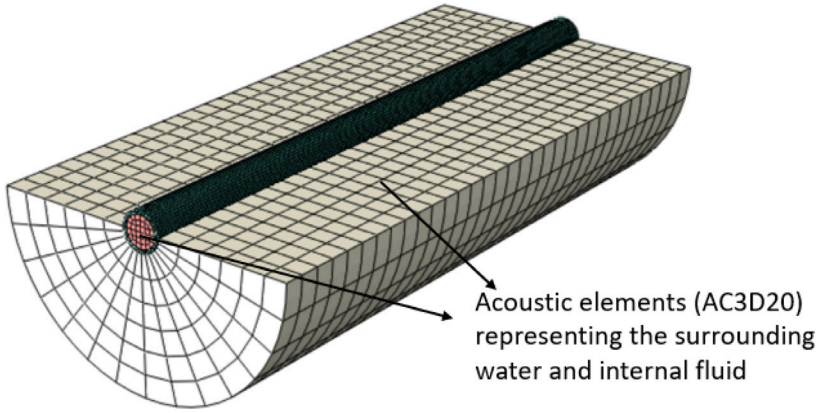

Fig. 3. FEM model of the submerged straight pipe.

The CASA cases involved two studies, one on the object in a vacuum and one on the acoustic elements representing the water domain. A final mesh scheme was selected based on these considerations.

3.1. Case I - A submerged straight pipe

Razi and Taheri (2014) presented a technique for detecting damage through vibrations, which they verified through numerical simulations and experimental testing. Before beginning the damage detection process, they conducted a laboratory experiment to test the accuracy of their numerical model. For this experiment, they suspended an aluminum pipe in a tank using soft elastic ropes, mimicking a free–free boundary condition. They then sent a chirp signal along the pipe using a piezoelectric transducer, while another piezoelectric sensor recorded the pipe's vibrations as a voltage signal. The numerical model used in the experiment was called CASA, and they applied fast Fourier transform (FFT) to the forced vibration signals obtained from both the experimental study and the model to determine the eigenvalues of the submerged line.

A model of a straight pipe was created in ABAQUS, as shown in Fig. 3 using 22000 linear hexahedral elements of type C3D8 and 33132 nodes. The translational degrees of freedom for the end elements of the pipe were restrained to ensure a clamped–clamped boundary condition. The main characteristics of the pipe can be found in Table 1.

ABAQUS's acoustic element AC3D20 was used to simulate the water. The surrounding medium and internal fluid were modeled using 5544 elements with 25508 nodes and 3200 elements with 4141 nodes, respectively. The water's density and bulk modulus values were 997 kg/m^3 and 2.13 GPa, respectively. A radiation boundary condition was used as an exterior boundary of the water to establish an effective water level depth (EWD). The radiation boundary condition was chosen to avoid reflecting the acoustic waves into the acoustic domain. The EWD was set to four times the outer diameter of the pipe, which was also the outer radius of the simulated water, based on the results from Razi and Taheri (2014).

Table 1
Main characteristics for the aluminum pipe.

Property	Value	Unit
Elastic modulus	68.9	GPa
Density	2700.0	kg/m^3
Poisson's ratio	0.3	–
Length	1.0	m
Outer diameter	60.0	mm
Wall thickness	5.2	mm

The first three eigenvalues of the submerged straight pipe were obtained via the simulated CASA and experimental approach and compared as tabulated in Table 2. The experimental and numerical results have minimal differences, confirming the reliability of using the CASA model on a submerged straight pipe.

In Table 2, all the first three eigenmodes correspond to lateral bending modes. In these modes, the pipe exchanges energy with the

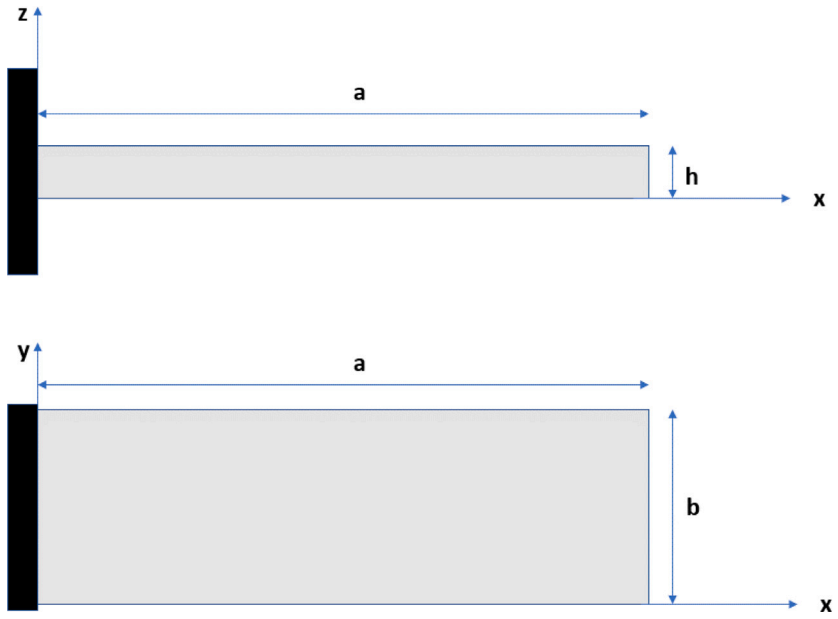

Fig. 4. Main dimension of the cantilever plate.
Source: Reproduced from Lindholm et al. (1962).

Table 2
Eigenfrequencies of the submerged straight pipe.

Mode	Present method [Hz]	Experimental [Hz]	% Difference
1	198.5	200.0	1
2	526.6	542.8	3
3	983.7	1030.6	5

Table 3
Wet eigenfrequencies of the straight pipe compared to dry.

Mode	Present method [Hz]	Air [Hz]	% Difference
1	198.5	335.1	51
2	526.6	877.0	50
3	983.7	1619	49

surrounding, making the added mass effects obvious, as shown in Table 3. CASA correctly simulates the mode shape order with reasonably predicted eigenfrequencies.

3.2. Case II - Submerged cantilever plates

Lindholm et al. (1962) conducted a study on the vibration of cantilever plates in water and air. They compared the results of fifteen submerged cantilevers to theoretical predictions using thin-plate and beam theories. They then adjusted these theories using chordwise hydrodynamic strip theory and an empirical correction factor to account for added mass in various modes (Chu, 1968). The cantilever plates they tested had varied plate aspect ratios (a/b) and thickness ratios (h/b) (from 1/2 to 5 and 0.009 to 0.124, respectively). The study provides each cantilever plate's natural frequencies of the first six modes.

Liang et al. (2001) studied submerged cantilever plates' vibration frequencies and mode shapes. They used an empirical added mass formula and the Rayleigh–Ritz method and compared their numerical findings to other relevant literature, including Lindholm's experimental results in air and water. The study found that the error remained almost constant at 5 % and 10 %, respectively.

Four of the fifteen submerged cantilever plates, as in Fig. 4, were chosen to test the CASA model. The plates were modeled with C3D20R elements (A 20-node quadratic brick with reduced integration Smith, 2009). The four chosen plates had the same width $b = 0.2032$ m, and their aspect and thickness ratios are shown in Table 4. The mechanical properties can be seen in Table 5.

Table 4
Aspect (a/b) and thickness (h/b) ratios of the four cantilever plates.

No	a/b	h/b [$\cdot 10^2$]
1	5	12.4
2	1	2.4
3	3	1.3
4	2	0.9

Table 5
Mechanical properties for the cantilever plates.

Mechanical property	Value	Unit
Elastic modulus	207	GPa
Density	7800	kg/m^3
Poisson's ratio	0.3	–

To figure out how much solid domain mesh refinement is needed, three mesh parameters (n_x, n_y, and n_z in Fig. 5) were varied for a dry case. The dry results were compared to the experimental results obtained by Lindholm et al. (1962). An approximate global seed size for the plates of 0.01 gave accurate dry results in all four cases. Using the CASA, according to Kramer et al. (2013), a relatively large water domain was chosen in the simulation. An approximate large size was selected to simulate the four cantilever plates in this study. The mesh parameters x_B/L, y_B/L, and z_B/L, shown in Fig. 6, became 0.5, 0.5 and 1.3, respectively. The approximate global seed size for the water domain was chosen as 0.05 with quadratic hexahedral elements of type AC3D20. Table 6 show the number of elements and nodes that simulate the water and cantilever plates.

Table 7 show that for cantilevers with high aspect ratios, the CASA model can capture results with an error percentage that remains nearly constant at 6 % for the first eigenmode and between 0.5% and 3 % for eigenmodes two and three in water compared to Lindholm's experimental results. For the shorter plates, the error percentages are between

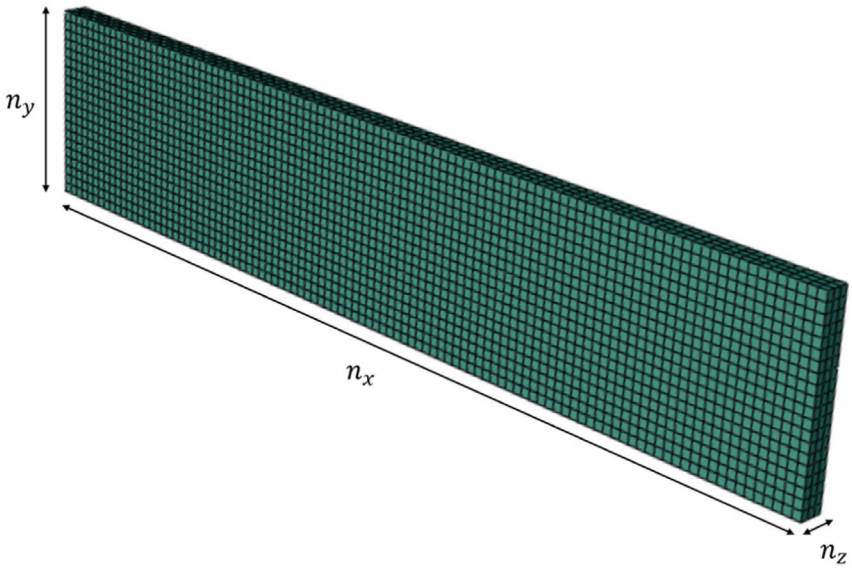

Fig. 5. Solid domain of plate No 1, described in Table 4.

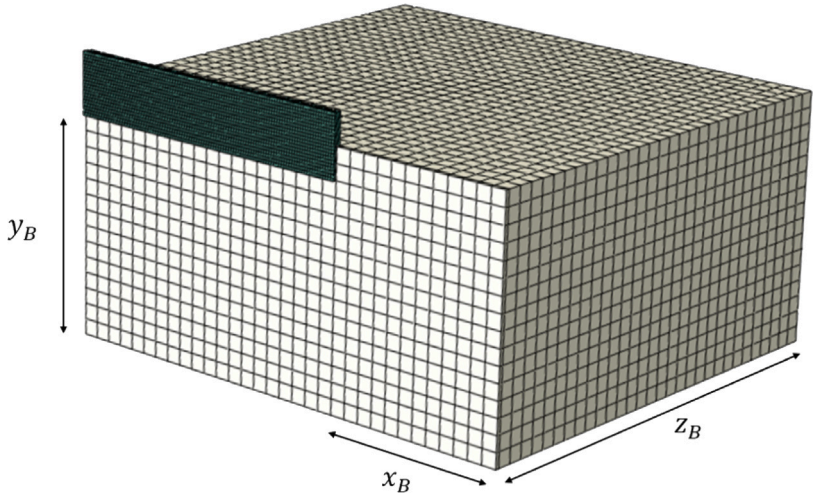

Fig. 6. Solid domain (green) of plate No 1, described in Table 4 and 1/4 of the fluid domain (white).

Table 6
Amount of elements and nodes used to simulate the four cantilever plates and water.

No	Plate		Water	
	Elements	Nodes	Elements	Nodes
1	6120	31 949	39 204	168 123
2	400	3003	400	2253
3	1220	8948	8472	38 233
4	820	6048	2816	13 429

Table 7
The present method CASA results compared to the Rayleigh–Ritz (RR) by Liang et al. (2001), and experimental (Exp) results from (Lindholm et al., 1962).

No	Mode 1			Mode 2			Mode 3		
	Present	RR	Exp	Present	RR	Exp	Present	RR	Exp
1	15.6	15.6	14.6	171.0	179.4	166.0	98.3	97.8	96.0
2	55.2	51.9	51.4	163.0	160.9	154.0	373.0	316.5	355.0
3	2.1	2.2	2.3	19.8	19.9	20.6	14.6	13.8	15.4
4	3.4	3.0	3.1	20.0	19.3	18.8	22.7	18.7	21.1

5 % and 7 % for all modes. According to Liang et al. (2001), the natural frequencies of all modes decrease with an increasing aspect ratio. Hence the added mass's effect is more pronounced. Understanding the natural vibration characteristics of structures through modal analysis is crucial, mainly when conducting wet modal analysis that considers the flow field's coupling effect. The eigenmodes are presented in Fig. 7. The first three eigenmodes are bending and twisting modes. Compared to the modes of the straight pipe, all the first three eigenmodes of the cantilever plates exchange energy with the surrounding water, showing that CASA can predict the first and most necessary eigenvalues.

3.3. Case III - A stiffened cylindrical shell

In a study conducted by Gao et al. (2022), the vibration and sound radiation of a typical stiffened cylindrical shell structure were measured under broadband excitation underwater. The results were compared to those obtained through the numerical finite element/boundary element (FE/BE) coupling method to ensure accuracy. Additionally, the researchers established testing procedures and operation steps to control vibration and sound radiation for an underwater vehicle. The

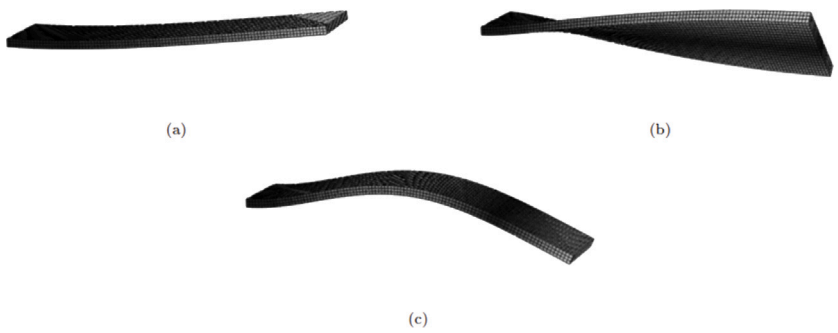

Fig. 7. First three modes of submerged cantilever plates. (**a**) First mode. (**b**) Second mode. (**c**) Third mode.

Fig. 8. The FE/BE model of the cylindrical shell, Gao et al. (2022) (**a**) Finite element model. (**b**) Boundary element model.

findings revealed that the test results were highly consistent with the FE/BE coupling method results. However, slight acceleration and sound pressure differences were observed at the resonance peak value in the 500–2500 Hz band.

The general FE/BE method adopted in the experiment to figure out the stiffened cylindrical shell's vibroacoustic characteristics, and the FE and BE model are shown in Fig. 8 (Gao et al., 2022). The EWD was set to four times the outer diameter of the cylindrical shell, with an approximate global mesh size of 0.02 m. This produced a total number of elements and nodes of 102976 and 147828, respectively. Water must be simulated at the ends because the cylindrical shell has closed ends. With the same approximate mesh size, 3440 elements and 5604 nodes were produced for the sides.

In Fig. 8a, the apparatus is placed 50 mm away from the center line of the cylindrical shell, and the stiffener sections are (80 x 10) mm with 450 mm spacing. A 1400 kg iron ballast was connected at the bottom of the cylindrical shell with rings and wires to balance gravity and buoyancy in the experiment (Gao et al., 2022). This created a simulation quality of 900 kg, which was reached by setting the steel density to 10100 kg/m^3. Table 8 show the material properties and dimensions. For the cylindrical shell, a total of 19180 quadratic hexahedral elements of type C3D20R and 10360 quadratic wedge elements of type C3D15 were used to minimize errors in the mesh. This produced 154850 nodes. C3D15 is a 15-node quadratic triangular prism and is often used together with hexahedrons when the geometry is too complicated to fill with hex elements only (Smith, 2009).

Fig. 9 shows six eigenmodes of the submerged stiffened cylindrical shell from Gao et al. (2022). The first, third, fourth and fifth modes all concern ovalities in the cylindrical shell. The second and sixth are stretching modes. How the stiffened cylindrical shell vibrates depends on its vibration modes, which affects how sound pressure is distributed when it is excited by a specific frequency (Gao et al., 2022). Table 9 shows the simulated CASA results compared to the results from Gao et al. (2022). Although their results were also obtained with an FE/BE method, it was concluded that the test results were in good agreement with those obtained by FE/BE coupling method. The presence of ring-stiffeners increases the stiffness of the entire structure, affecting the stiffness of smaller parts and increasing the likelihood of axial modes. The CASA model accurately simulated the first six eigenmodes, even though none were bending, twisting, or torsional modes.

Table 8
Mechanical properties and dimensions for the stiffened cylindrical shell.

Mechanical properties	Value	Unit
Elastic modulus	210.0	GPa
Density	10.1	t/m^3
Poisson's ratio	0.3	–
Length	1.8	m
Radius	0.6	m
Wall thickness	10.0	mm

Table 9
Comparison of CASA results with experimental results from Gao et al. (2022) of the submerged stiffened cylindrical shell.

Mode	Present method [Hz]	FE/BE results from Gao et al. (2022) [Hz]	% Difference
1	192	178	8
2	205	210	3
3	251	257	2
4	257	266	3
5	287	282	2
6	395	395	0

3.4. Case IV - A submerged disk

Valentín et al. (2017) examined a disk connected to a shaft and placed in a water tank. Pressure sensors were placed on the cover to measure the pressure variations caused by the disk's vibration, while accelerometers were installed on both the disk and the cover. The team analyzed signals from the hammer, accelerometers, and pressure

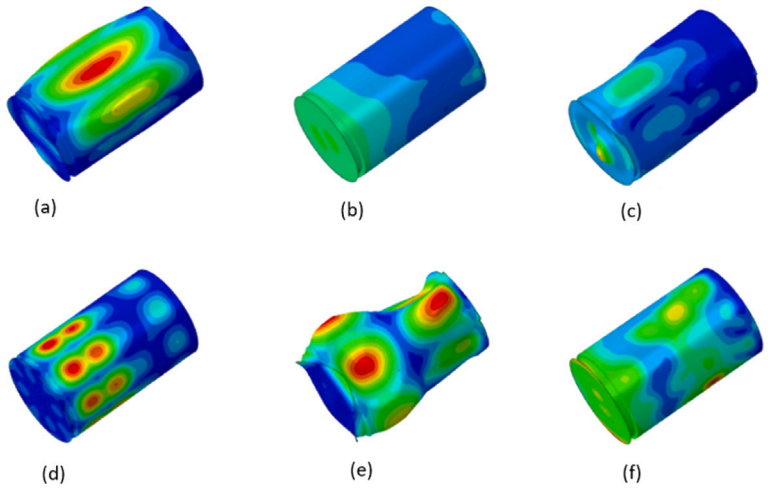

Fig. 9. Six mode shapes of submerged stiffened cylindrical shell. (**a**) Mode 1. (**b**) Mode 2. (**c**) Mode 3. (**d**) Mode 4. (**e**) Mode 5. (**f**) Mode 6. *Source:* Taken from Gao et al. (2022).

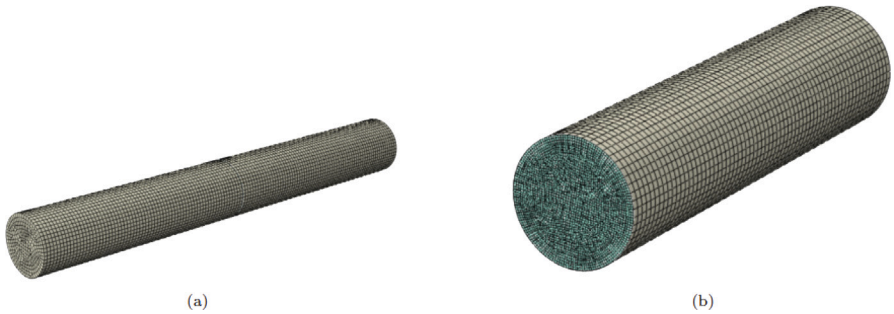

Fig. 10. Visual of the meshed CASA model of the submerged disk. (**a**) The full CASA model. (**b**) The disk with one of the water domains.

Table 10
Mechanical properties and dimensions of the submerged disk.

Property	Value	Unit
Radius	125	mm
Thickness	3	mm
Disk density	7800	kg/m^3
Elastic modulus	207	GPa
Poisson's ratio	0.3	–

Table 11
Eigenvalues of the disk in water.

n	Present method [Hz]	Experimental [Hz]	% Difference
2	116	145	20
3	304	310	2
4	577	580	1
5	938	900	4
6	1386	1390	0

sensors. Air tests using the roving hammer impact method determined the disk's mode shapes.

The test rig utilized a stainless steel disk connected to a shaft and placed in an aluminum tank filled with water. The disk could move up and down along the shaft, which allowed researchers to analyze how the nearby rigid surface of the bottom (H_2) and top cover (H_1) affected it. The dimension and material properties are in Table 10.

Our CASA model involved positioning the disk with a distance of four times its diameter from the bottom surface and top cover. The water mesh generated 19765 quadratic hexahedral elements of type AC3D20 and 402 quadratic wedge elements of type AC3D15 with an approximate global mesh size of 0.015 m, producing 86375 nodes. An approximate mesh size of 0.005 m for the disk generated 2377 quadrilateral elements of type S8R and 28 quadratic triangular elements of type STRI65, resulting in 7344 nodes. When coupling fluids to both sides of shell or beam elements, the mesh for the medium with the lower wave speed should be the slave surface in a "Tie" constraint. In the case of our model, the fluid was coupled to both sides of S8R and STRI65 shell elements, so the master and slave surfaces were appointed to the fluid and disk, respectively. The meshed model can be seen in Fig. 10, with the disk clamped at its center to simulate the experiment's shaft.

The behavior of an underwater disk is greatly influenced by the added mass and damping effects, along with the distance from solid boundaries. In previous cases, the CASA has proven a trustworthy approach for simulating mode shapes with significant added mass influence. In Valentín et al. (2017), the natural frequencies and mode shapes found within the testing frequency band were configurations where the added mass effect had less influence. The mode shapes of the disk had no nodal circles ($m = 0$). The only modes Valentín et al. (2017) studied were the mode shapes with nodal diameters (n) because they were most prone to excitement. $n = 0$ and $n = 1$ were not selected due to the boundary effects. Therefore, modes $n = 2$ to $n = 6$ are the only ones considered. The modes can be seen in Fig. 11.

Table 11 shows that the CASA model cannot accurately capture the first eigenvalue when the submerged object is a disk. The first eigenvalue produced by CASA has an error percentage of 19.71%, while the rest have error percentages between 0.28% and 4.20%. In the experimental article by Valentín et al. (2017), the disk and water had no mechanical properties, density, or bulk modulus. Furthermore, the experiment is conducted with different cover distances and different

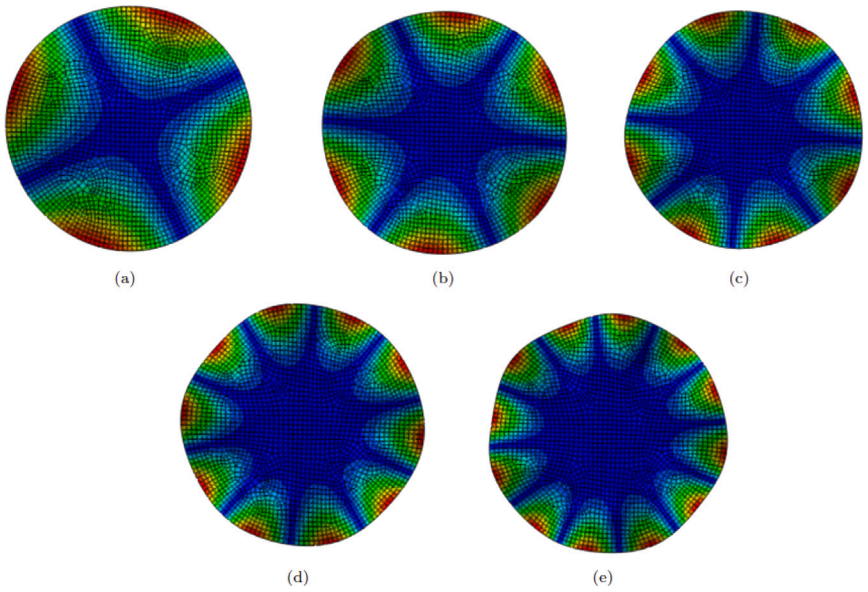

Fig. 11. Modal shapes of the submerged disk, presented by its number of nodal diameters (n). **(a)** $n = 2$.**(b)** $n = 3$. **(c)** $n = 4$. **(d)** $n = 5$. **(e)** $n = 6$.

thicknesses of the covers. Multiple methods, such as the hammer signal and pressure sensors, were used to capture the natural frequencies. Both these methods yielded different results. The factors above contribute to producing different experimental results, which may be the cause of the low accuracy of the first CASA mode. However, CASA gives good predictions for higher modes.

4. Application cases to submerged subsea jumpers

The previous section successfully applied CASA as a modal analysis approach to various submerged geometries. These geometries are relevant to subsea jumpers, as they mimic essential features encountered in jumper's geometry. The validation cases underscore the versatility and accuracy of CASA for assessing the dynamic behavior and structural integrity of the subsea jumper and its components.

Typically, commercial software simulates subsea jumpers using beam elements. However, recent findings suggest that this approach may lead to incorrect predictions of free vibration modes due to the presence of bends (Sieber et al., 2021). This section is based on the findings in Ullestad (2023), and presents two application cases of 3D subsea rigid jumpers with bends to accurately predict free vibration modes and reasonably estimate eigenfrequencies.

4.1. Case I - A single planar subsea jumper

ExxonMobil (Wang et al., 2013) conducted tests using a model of a shaped jumper to investigate how to predict VIV. This model's scaled arch length was 13.96 m, and the ratio was 4.525. The test aimed to determine whether VIV occurs at low velocities in realistic flow conditions. A one-meter straight cylinder section was also used to measure drag forces and assess sensitivity to Reynolds number changes. On the jumper model, thirteen tri-axial accelerometers and three strain gauges were placed to record different flow angles and current velocities. The results showed that VIV occurred at specific towing speeds and frequencies, and response amplitudes were given for all accelerometers. The test set is depicted in Fig. 12.

ExxonMobil experimented using a thin-walled aluminum pipe for the model jumper. This resulted in a relatively less massive model than the thick-walled steel prototype (Wang et al., 2013). Low-density oil, high-density sugar, and lead weights were added and evenly distributed along the length to increase the model's mass. As a result, the mass ratio of the model increased to 2.33. The lengths of the model can be found

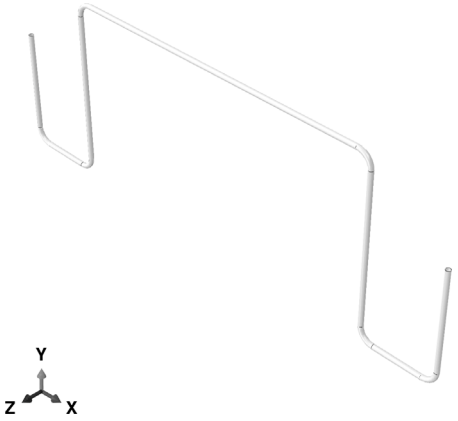

Fig. 12. Jumper model.

Table 12
Lengths of the vertical (V) and horizontal (H) segments in the jumper model.

Name	Length [m]
V 1	1.495
H 1	1.000
V 2	2.323
H 2	4.327
V 3	2.323
H 3	1.000
V 4	1.495
Total length	13.96

Table 13
Jumper simulation model properties.

Parameter	Value	Unit
Total length	13.50	m
Unit mass	6.66	kg/m
Outer diameter	60.50	mm
Inner diameter	55.00	mm
Elastic modulus	69.00	GPa
Shear modulus	26.10	GPa

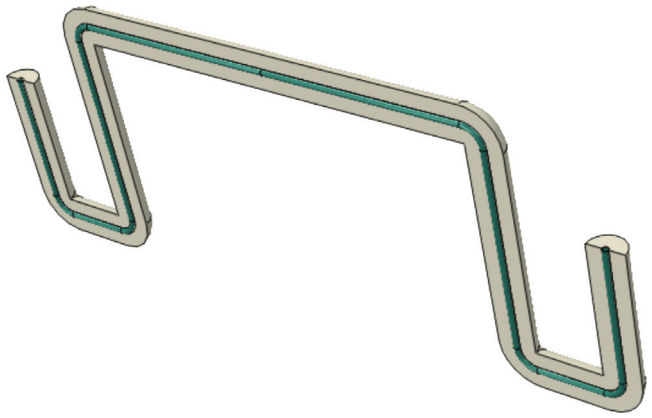

Fig. 13. Assembly model of the M-shaped jumper and 1/2 of the water domain.

in Table 12, while the properties of the simulated jumper model are listed in Table 13.

Sieber et al. (2021) used the jumper in Fig. 12 to test the Elbow31B model to the PIPE31 model in ABAQUS. The PIPE31 model assumes plane stress and considers all degrees of freedom (DOF) except for hoop stresses and hoop strains, which are accounted for using shell theory. On the other hand, the Elbow31B model is a bend element based on Bathe's approach (Bathe et al., 1983), which considers cross-sectional deformation and kinematic non-linearity. The cross-sectional deformation in the jumper model is due to the bending of a straight pipe during manufacturing.

According to Sieber et al. (2021), Elbow31B models generally produce lower results than PIPE31 models. Eigenmode two and three were switched in order, where the Elbow31B results correlated with the observations from the model test done by ExxonMobil. This highlights the importance of using elbow elements for analyzing subsea jumpers and obtaining accurate mode shapes and frequencies.

For the simulated scenario, the 90° corners were modeled as curved fillets. As the bending radius was three times the outer diameter of the pipe, the arch length was 0.285 m, and the bending radius was 0.182 m. This decreased the model's total size, compared to the dimensions used by ExxonMobil in Table 12, to 13.496 m. From Table 13, the total mass of the jumper becomes 89.9 kg. The material density was increased to reach this mass magnitude in the simulation. With solid elements, ABAQUS calculated the pipe volume to be 0.00673 m^3, making the material density 13349 kg/m^3.

In our CASA model of the M-shaped jumper, the EWD was set to three times the outer diameter of the pipe. The bends of the model were equal to three times the outer diameter, forcing the EWD to be equal or less. Fig. 13 show the assembly model of the CASA model. The jumper comprises 26920 quadratic hexahedral elements of type C3D20 and 188540 nodes. The water surrounding the pipe is modeled by 244509 quadratic tetrahedral elements of type AC3D10, connected by 356869 nodes. Fig. 14 shows the finite element model of the jumper.

Table 14 compares the first three eigenmodes obtained from CASA and Sieber's results for the submerged jumper. Based on the data presented in the table, the first three eigenvalues obtained from both approaches show a reasonable level of agreement, indicating that the CASA model is reliable. Additionally, the eigenmodes from the Elbow31B model align well with the results observed by ExxonMobil and exhibit a good correlation with the CASA model. The first mode is out-of-plane bending, while the second is in-plane bending. The third mode is an out-of-plane twist, which can be viewed in Figs. 15–17. These findings offer a strong foundation for trusting the CASA model, provided it is appropriately utilized.

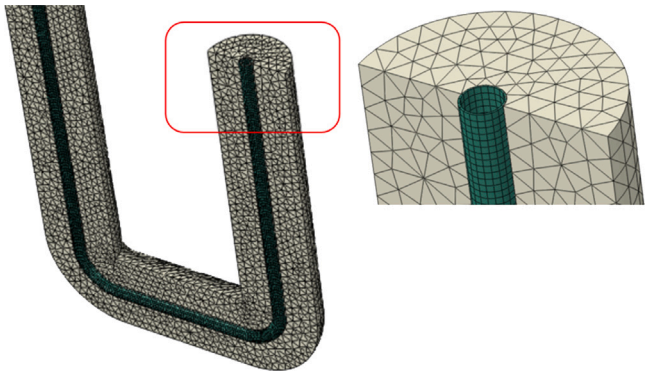

Fig. 14. Mesh element model of the M-shaped jumper.

Table 14
Comparison of the first three eigenfrequencies and mode shapes estimated (Sieber et al., 2021) Pipe34 model and CASA (Sieber et al., 2021).

Mode	Present method [Hz]	FE results from Sieber et al. (2021) [Hz]	% Difference
1	0.8457	0.8336	1.4
2	1.9878	1.9406	2.4
3	2.1623	2.1344	1.3

Table 15
Parameters of the jumper model.

Parameter	Value	Dimension
Outer diameter	52.0	mm
Wall thickness	2.00	mm
S1, S2, S6, S7	0.50	m
S3, S5	0.80	m
S4	2.00	m
Density	7850	kg/m^3
Poisson's ratio	0.30	–
Young's Modulus	206	GPa

4.2. Case II - A multi-planar subsea jumper

Li et al. (2022) conducted a study examining the gas-liquid flow and resulting vibrations in a multi-planar subsea jumper. They used numerical and experimental approaches, installing sensors near the elbows to measure pressure and vibration responses. The researchers could identify various flow patterns and vibrations induced at different gas and liquid velocities by conducting numerical simulations that analyzed the one-way coupling between fluids and solids and compared the results to experimental data. The jumper model and parameters are in Fig. 18 and Table 15, respectively.

The bends were modeled as three times the outer diameter, resulting in a bending radius equal to 0.156 m and an arch length of 0.245 m. The total length of the jumper was 4.898 m. The approximate global mesh size for the jumper was 0.002 m, creating 204926 linear hexahedral elements of type C3D8 and 410010 nodes. For the water domain, the EWD was three times the outer diameter, just as the bending radius. The approximate global mesh size was 0.015 m, creating 682718 quadratic tetrahedral elements of type AC3D10 and 962324 nodes. The bulk modulus and water density were set to 2.13 GPa and 1000 kg/m^3, respectively.

The ABAQUS/Aqua option can be utilized to analyze beam-like structures installed underwater and subjected to loading by water and wave actions for offshore structures. ABAQUS/Aqua offers specific features designed for this purpose, including modeling buoyancy, ballast, added mass, waves, and current loads (Rønnquist et al., 2020). PIPE31 elements were used to create the ABAQUS/Aqua model. However, ABAQUS cannot apply added mass to a beam structure with bends. Therefore, the PIPE31-model was modeled as shown in Fig. 18. For

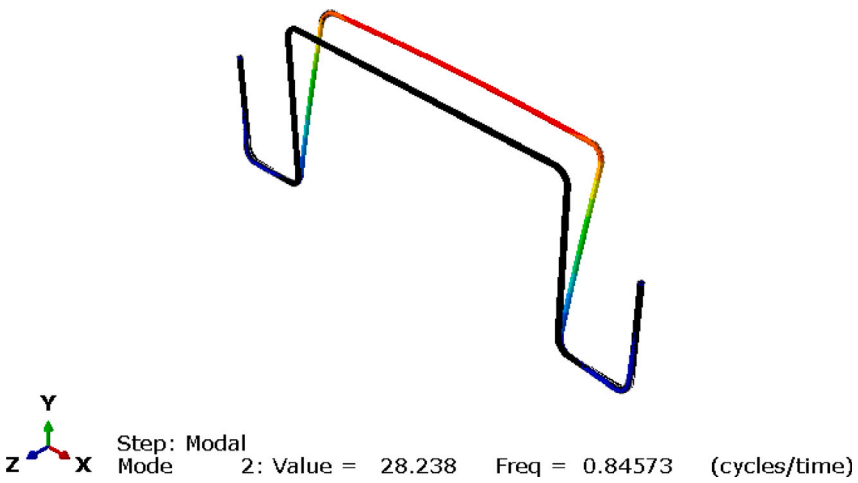

Fig. 15. Mode one of the submerged M-shaped jumper. The largest displacement is at the top horizontal segment, an out-of-plane bending mode.l.

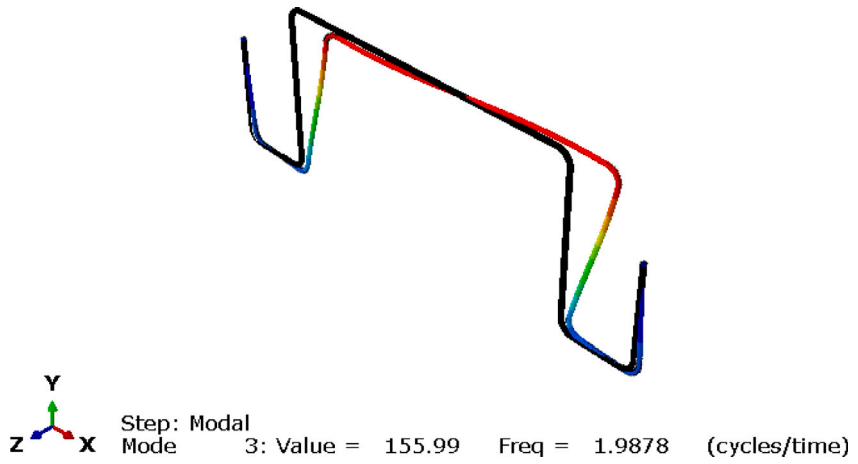

Fig. 16. Mode two of the submerged M-shaped jumper. X-axis in-plane bending.

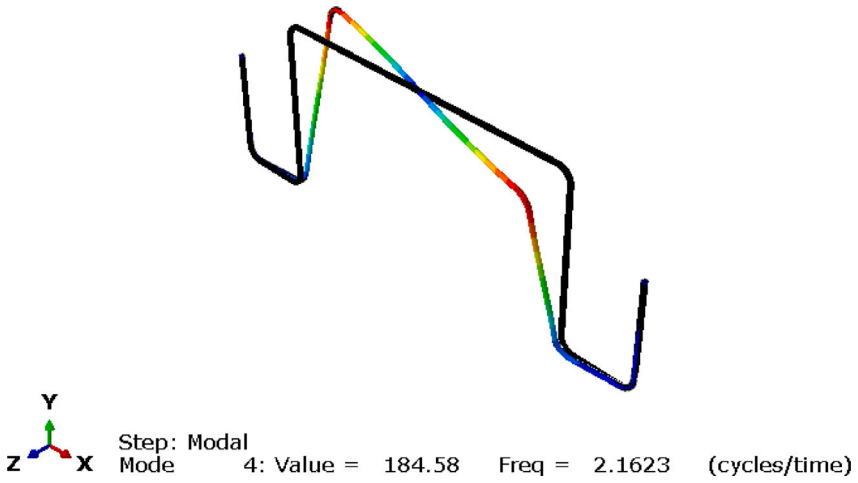

Fig. 17. Mode three of the submerged M-shaped jumper. Out-of-plane twist.

the PIPE31 model, the global mesh size was approximately equal to the outer diameter, 0.052 m, creating 108 linear line elements of type PIPE31 and 109 nodes.

Another way to apply added mass to structures in ABAQUS is to use the "nonstructural mass" option. This method is more straightforward than adding a group of point masses. The added mass applied to the structure can be calculated using the equation Eq. (17).

$$m_{added} = \rho_f \pi \frac{D^2}{4} L \tag{17}$$

Where m_{added} is the total added mass, ρ_f is the fluid density, D is the outer diameter of the jumper, L is the total length of the jumper.

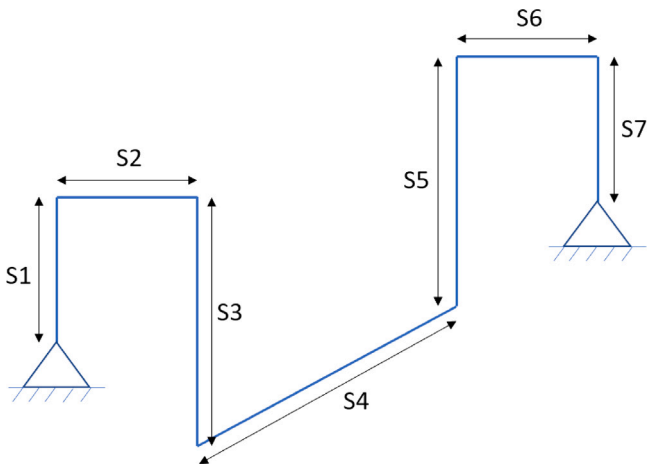

Fig. 18. Detailed jumper model.

Table 16
The first five eigenfrequencies simulated with CASA, ABAQUS/Aqua, and nonstructural mass, in ABAQUS for the 3D-jumper, presented in Li et al. (2022).

Mode	Present method	ABAQUS/Aqua (PIPE31)	Nonstructural mass(B31)
1	8.642	13.68	11.50
2	17.27	24.40	20.64
3	17.48	19.51	17.19
4	26.48	35.81	32.16
5	32.09	38.29	33.02

B31 (A 2-node linear beam in space Smith, 2009) elements were used to mesh the model. The approximate global mesh size for the beam model was equal to the outer diameter, 0.052 m, creating 102 linear line elements of type B31 and 103 nodes. By applying added mass with "nonstructural mass", the model can contain bends. As with the CASA model, the bends were modeled as three times the outer diameter, resulting in a bending radius of 0.156 m and an arch length of 0.245 m. The total length of the jumper was 4.898 m. The simulated eigenfrequencies are presented in Table 16.

Table 16 show that the CASA results differ vastly from those simulated with beam elements. The difference in the first eigenvalue between PIPE31 and CASA is quite significant, with a relative error of over 45 %. Additionally, the beam models show a switch in the second and third eigenmodes compared to the CASA model. The second and third modes have similar eigenfrequencies in the CASA model, which could explain the switch. However, the nonstructural mass model offers reasonable results in the third and fifth modes when compared to CASA. The third mode involves displacement in the z-direction, while the fifth mode is related to bending in the x-direction and twisting around the x-axis. The nonstructural mass model has maximum errors of about 3 % in these modes, while the ABAQUS/Aqua model has up to 34 %. The mode shapes of the multi-planar jumper are shown in Figs. 19–23.

The ABAQUS/Aqua and nonstructural mass approach use the equation found in Eq. (17) to distribute fluid inertia loading. The equation used here is based on Blevins' added mass term, originally designed to analyze the vibrations of a submerged beam (Blevins, 2001). However, the results presented in Table 16 indicate that the multi-planar jumper behaves more like a shell structure than a beam. The jumper is modeled differently in dynamic analysis depending on the approach used. The jumper is modeled with a constant cross-section and thickness when using beam elements, while the CASA approach utilizes solid elements to account for parameter changes. It is crucial to consider changes in cross-section and thickness for the multi-planar jumper, as the structure becomes less stiff and the eigenfrequencies decrease.

In modal analysis, a structure's natural frequencies and mode shapes are of interest. These characteristics depend on how the structure deforms under its mass and stiffness distribution. For the multi-planar subsea jumper, shell elements can capture the bending and membrane effects that influence the modal behavior. Solid elements inherently account for these effects because they are three-dimensional, and shell elements approximate these behaviors more closely than beam elements. Beam models often assume a uniform cross-sectional stiffness, which may lead to inaccuracies in modal analysis. Therefore, in terms of its modal behavior and characteristics, the jumper behaves more like a shell structure than a beam.

5. Discussion on the cost-effectiveness of CASA method

The CASA is modeled with solid elements. Solid elements are well-suited for analyzing complex, irregular geometries. They can capture the 3D nature of the structure and provide accurate results for such cases. Acoustic elements are used in conjunction with solid elements to study the acoustic behavior of the fluid surrounding the submerged object. The meshing of solid geometries can be challenging and not straightforward.

Beam elements are ideal for linear elastic materials and structures with uniform cross-sections. They are well-suited for long and slender geometries like line pipes. However, they are unsuitable for modeling 3D effects, such as bending out-of-plane, torsion, or complex deformations.

As to the computation demands, the CASA requires much more time due to the model containing a significant degree of freedom. All simulations in this study have been performed on a standard laptop PC

Fig. 19. Mode one of the multi-plane jumper. Displacement in the x-direction.

Fig. 20. Mode two of the multi-plane jumper. Twist about the *y*-axis.

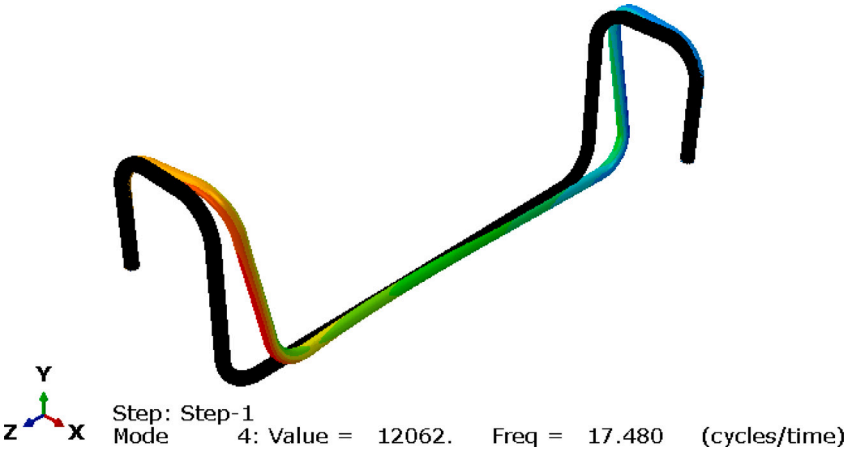

Fig. 21. Mode three of the multi-plane jumper. Displacement in the *z*-direction.

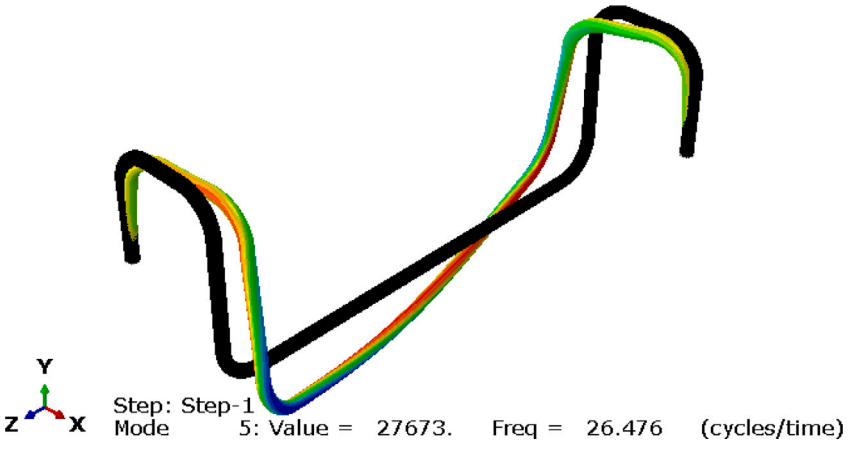

Fig. 22. Mode four of the multi-plane. Twisting about the *y*-axis and bending in the *y*-direction.

(AMD Ryzen™7 4700U and 16 G RAMP). The longest running time is about 4 h for the multi-planar model. If a high-performance PC is used instead, the computation time could be significantly lower. In contrast, the beam-based model can be solved in seconds, but the accuracy of the results might be in doubt, especially for complicated 3D jumper structures.

6. Conclusions

In this study, we presented a thorough evaluation of the CASA model in doing the modal analysis for submerged structures. Experimental tests have been used for validation. Additionally, two application cases have also been successfully simulated. The following conclusions have been made

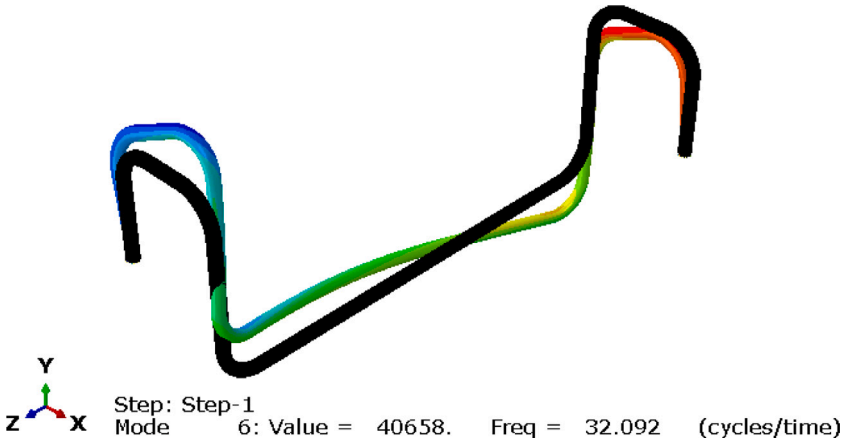

Fig. 23. Mode five of the multi-plane jumper. Bending in the x-direction and twisting about the x-axis.

- The CASA simulations were compared well with published experimental results in the verification cases. The exception is the comparisons between the CASA and experimental results for the first eigenvalue when the submerged object is a disk. In this mode shape, the disk had two nodal diameters ($n = 2$) and no nodal circles ($m = 0$), and the error percentage was 20 %.
- The CASA simulates eigenfrequencies that closely match the experimental results for mode shapes that involve significant energy exchange with the surrounding water. For example, the error percentages for the lateral bending modes of the straight pipe are under 2 %. For the cantilever plates, the error margins are a maximum of 6 % and 7 % for twisting and bending modes, respectively. Generally speaking, it is shown that the CASA method gives more reliable modal analysis results.
- For the two application cases, the CASA predicts a different order of mode shapes than beam elements, building on the statement that beam elements may give the wrong prediction of the free vibration modes due to bends. The mode shape order of the M-shaped jumper correlates with the observations done by Exxon-Mobil, and the eigenfrequencies are in reasonable agreement with the results obtained by Sieber et al. (2021). For the multi-planar jumper, mode shapes two and three, simulated by CASA, are switched in order compared to the beam models. The CASA eigenfrequencies are also vastly different from the beam elements, with error values up to 45 %. Consequently, it is not recommended to run beam models for the multi-planar subsea jumpers or similar submerged structures.
- The method with adding mass to beam elements is significantly more cost-effective than CASA. In addition to the computational cost, modeling complex geometries with the CASA can be challenging. But when the geometry of pipe-like structures contains multiple bends and becomes multi-planar, like subsea jumpers and spools, CASA has proven itself to produce more reliable results than adding mass to beam elements.

CRediT authorship contribution statement

Oskar Ask Ullestad: Conceptualization, Methodology, Software, Validation, Formal analysis, Investigation, Writing – original draft, Writing – review & editing, Visualization. **Zhenhui Liu:** Conceptualization, Methodology, Formal analysis, Investigation, Writing – review & editing, Supervision.

Declaration of competing interest

The authors declare that they have no known competing financial interests or personal relationships that could have appeared to influence the work reported in this paper.

Data availability

Data will be made available on request.

Acknowledgments

We thank the Department of Machine and Marine (IMM) at Western Norway University of Applied Science (HVL) for financial support for this research. In addition, Professor Bjørn Tore Hjertaker from the University of Bergen (UiB) and Dr. Guang Yin from the University of Stavanger (UiS) have been given good advice during this research work and are highly acknowledged. Finally, we thank Aker Solutions for allowing us to publish this work.

References

Bak, S., Yoo, J., 2019. FSI analysis on the sail performance of a yacht with rig deformation. Int. J. Naval Architect. Ocean Eng. 11, http://dx.doi.org/10.1016/j.ijnaoe.2019.02.003.

Bao, C., Hao, H., Li, Z., 2013. Vibration-based structural health monitoring of offshore pipelines: Numerical and experimental study. Struct. Control Health Monit. 20, http://dx.doi.org/10.1002/stc.1494.

Bathe, K.-J., Almeida, C.A., Ho, L.W., 1983. A simple and effective pipe elbow element—some nonlinear capabilities. In: Bathe, K. (Ed.), Nonlinear Finite Element Analysis and Adina. Pergamon, pp. 659–667. http://dx.doi.org/10.1016/B978-0-08-030566-0.50009-6, URL https://www.sciencedirect.com/science/article/pii/B9780080305660500096.

Blevins, R., 2001. Flow-Induced Vibration. Krieger Publishing Company, URL https://books.google.no/books?id=Wzo8PgAACAAJ.

Chae, H., Kim, C., 2010. A numerical study with FSI mode on the characteristics of pressure fluctuation and discharge valve motion in rotary compressors with single and dual muffler. Int. J. Precis. Eng. Manuf. 11, 589–596. http://dx.doi.org/10.1007/s12541-010-0068-2.

Chen, J., Su, Z., 2009. Identification of corrosion damage in submerged structures using fundamental anti-symmetric lamb waves. Smart Mater. Struct. 19, 015004. http://dx.doi.org/10.1088/0964-1726/19/1/015004.

Cheng, X., Zhao, L., Zhao, Y., Zhang, A., 2015. Fsi resonance response of liquid-storage structures made of rubber-isolated rectangular reinforced concrete. Electron. J. Geotech. Eng. 20, 1809–1824.

Chu, W.H., 1968. Vibrations of fully submerged cantilever plates in water. Schiffstechnik 15 (78), URL https://repository.tudelft.nl/islandora/object/uuid%3Abbd2ee9a-e527-4b51-8890-7dd12c7e5244.

Fourey, G., Hermange, C., Le Touzé, D., Oger, G., 2017. An efficient FSI coupling strategy between smoothed particle hydrodynamics and finite element methods. Comput. Phys. Comm. 217, http://dx.doi.org/10.1016/j.cpc.2017.04.005.

Fujita, K., 1990. Flow-induced vibration and fluid-structure interaction in nuclear power plant components. J. Wind Eng. Ind. Aerodyn. 33 (1), 405–418. http://dx.doi.org/10.1016/0167-6105(90)90056-I, URL https://www.sciencedirect.com/science/article/pii/016761059090056I.

Gao, C., Zhang, H., Li, H., Pang, F., Wang, H., 2022. Numerical and experimental investigation of vibro-acoustic characteristics of a submerged stiffened cylindrical shell excited by a mechanical force. Ocean Eng. 249, 110913. http://dx.doi.org/10.1016/j.oceaneng.2022.110913, URL https://www.sciencedirect.com/science/article/pii/S0029801822003493.

Hellgren, R., 2014. Influence of Fluid Structure Interaction on a Concrete Dam during Seismic Excitation: -Parametric analyses of an Arch Dam-Reservoir-Foundation system (Ph.D. thesis).

Kramer, M.R., Liu, Z., Young, Y.L., 2013. Free vibration of cantilevered composite plates in air and in water. Compos. Struct. 95, 254–263. http://dx.doi.org/10.1016/j.compstruct.2012.07.017, URL https://www.sciencedirect.com/science/article/pii/S0263822312003455.

Li, W., Zhou, Q., Yin, G., Ong, M.C., Li, G., Han, F., 2022. Experimental investigation and numerical modeling of two-phase flow development and flow-induced vibration of a multi-plane subsea jumper. J. Marine Sci. Eng. 10 (10), http://dx.doi.org/10.3390/jmse10101334, URL https://www.mdpi.com/2077-1312/10/10/1334.

Liang, C.-C., Liao, C.-C., Tai, Y.-S., Lai, W.-H., 2001. The free vibration analysis of submerged cantilever plates. Ocean Eng. 28 (9), 1225–1245. http://dx.doi.org/10.1016/S0029-8018(00)00045-7, URL https://www.sciencedirect.com/science/article/pii/S0029801800000457.

Lindholm, U.S., Kana, D.D., Chu, W.-H., Abramson, H.N., 1962. Elastic vibration characteristics of cantilever plates in water. J. Ship Res. 9, 11–36.

Liu, Z., Igeh, L., Wu, J., Ong, M., 2019. Fatigue damage assessment to a rigid planar jumper on model scale. J. Offshore Mech. Arct. Eng. 142, 1. http://dx.doi.org/10.1115/1.4044074.

Peng, X.-l., Hao, H., 2012. A numerical study of damage detection of underwater pipeline using vibration-based method. Int. J. Struct. Stab. Dyn. 12, http://dx.doi.org/10.1142/S0219455412500216.

Peng, X.-L., Hao, H., Li, Z.-X., 2012. Application of wavelet packet transform in subsea pipeline bedding condition assessment. Eng. Struct. 39, 50–65. http://dx.doi.org/10.1016/j.engstruct.2012.01.017, URL https://www.sciencedirect.com/science/article/pii/S0141029612000570.

Razi, P., Taheri, F., 2014. A vibration-based strategy for health monitoring of offshore pipelines' girth-welds. Sensors 14 (9), 17174–17191. http://dx.doi.org/10.3390/s140917174, URL https://www.mdpi.com/1424-8220/14/9/17174.

Razi, P., Taheri, F., 2015. On the vibration simulation of submerged pipes: Structural health monitoring aspects. J. Mech. Mater. Struct. 10, 105–122. http://dx.doi.org/10.2140/jomms.2015.10.105.

Rønnquist, N.E.A., Perotti, F., Martinelli, L., 2020. Global Analysis of Submerged Floating Tunnels Under Hydrodynamic Loading. Norwegian University of Science and Technology, https://hdl.handle.net/11250/2780048.

Ross, C.T., Kster, P., Little, A.P., Tewkesbury, G., 2007. Vibration of a thin-walled prolate dome under external water pressure. Ocean Eng. 34 (3), 560–575. http://dx.doi.org/10.1016/j.oceaneng.2006.01.013, URL https://www.sciencedirect.com/science/article/pii/S0029801806001181.

Sieber, L., Liu, Z., Sævik, S., Ringsberg, J., 2021. Assessment of Vortex-Induced Vibration fatigue of subsea template jumper by using a time domain model. Norwegian University of Science and Technology, https://hdl.handle.net/11250/2989641.

Smith, M., 2009. ABAQUS/Standard User's Manual, Version 6.9. Dassault Systèmes Simulia Corp, United States.

Ullestad, O.A., 2023. A comparative study on the free vibration characteristics of submerged pipe structures. University of Bergen, https://hdl.handle.net/11250/3070620.

Valentín, D., Presas, A., Egusquiza, E., Valero, C., Egusquiza, M., 2017. Experimental study of a vibrating disk submerged in a fluid-filled tank and confined with a nonrigid cover. J. Vib. Acoust. 139 (2), 021005. http://dx.doi.org/10.1115/1.4035105, arXiv:https://asmedigitalcollection.asme.org/vibrationacoustics/article-pdf/139/2/021005/6348304/vib_139_02_021005.pdf.

Wang, H., Huang, J., Lee, S., Gioielli, P., Kan, W., Spencer, D., Islam, M., 2013. VIV response of a subsea jumper in uniform current. In: International Conference on Offshore Mechanics and Arctic Engineering, Volume 4B: Pipeline and Riser Technology, V04BT04A043. http://dx.doi.org/10.1115/OMAE2013-11417, arXiv:https://asmedigitalcollection.asme.org/OMAE/proceedings-pdf/OMAE2013/55379/V04BT04A043/2524562/v04bt04a043-omae2013-11417.pdf.

Zeinoddini, M., Parke, G., Sadrossadat, M., 2012. Free-spanning submarine pipeline response to severe ground excitations: Water-pipeline interactions. Pipeline Syst. Eng. Pract. 3, http://dx.doi.org/10.1061/(ASCE)PS.1949-1204.0000098.

Zhu, X.Q., Hao, H., Peng, X.L., 2008. Dynamic assessment of underwater pipeline systems using statistical model updating. Int. J. Struct. Stab. Dyn. 08 (02), 271–297. http://dx.doi.org/10.1142/S021945540800265X.

Zienkiewicz, O.C., 2005. The finite element method : its basis and fundamentals, sixth ed. Elsevier Butterworth-Heinemann, Amsterdam.

Zou, G., Cheraghi, N., Taheri, F., 2005. Fluid-induced vibration of composite natural gas pipelines. Int. J. Solids Struct. 42 (3), 1253–1268. http://dx.doi.org/10.1016/j.ijsolstr.2004.07.001, URL https://www.sciencedirect.com/science/article/pii/S0020768304004123.